PHYSICAL REVIEW LETTERS **134,** 183406 (2025)

Thermodynamics of Spin-Imbalanced Fermi Gases with SU(N)-Symmetric Interaction

Chengdong He,[1,2,*] Xin-Yuan Gao,[3,*] Ka Kwan Pak,[1] Yu-Jun Liu,[1] Peng Ren,[1,2] Mengbo Guo,[1]
Entong Zhao,[1] Yangqian Yan,[3,4,†] and Gyu-Boong Jo[1,2,‡]
[1]*Department of Physics, The Hong Kong University of Science and Technology, Clear Water Bay, Kowloon, Hong Kong, China*
[2]*Department of Physics and Astronomy, Rice University, Houston, Texas 77005, USA*
[3]*Department of Physics, The Chinese University of Hong Kong, Shatin, Hong Kong, China*
[4]*The Chinese University of Hong Kong Shenzhen Research Institute, Shenzhen 518000, China*

(Received 27 August 2024; revised 24 March 2025; accepted 10 April 2025; published 7 May 2025)

Thermodynamics of degenerate Fermi gases has been extensively studied through various aspects such as Pauli blocking effects, collective modes, BCS superfluidity, and more. Despite this, multicomponent fermions with imbalanced spin configurations remain largely unexplored, particularly beyond the two-component scenario. In this Letter, we generalize the thermodynamic study of SU(N) fermions to spin-imbalanced configurations based on density fluctuations. Theoretically, we provide closed-form expressions of density fluctuation across all temperature ranges for general spin population setups. Experimentally, after calibrating the measurements with deeply degenerate ^{173}Yb Fermi gases under spin-balanced configurations ($N \leq 6$), we examine the density fluctuations in spin-imbalanced systems. Specifically, we investigate two-species and four-species configurations to validate our theoretical predictions. Our analysis indicates that interaction enhancement effects can be significant even in highly spin-imbalanced systems. Finally, as an application, we use this approach to examine the decoherence process. Our Letter provides a deeper understanding of the thermodynamic features of spin-imbalanced multicomponent Fermi gases and opens new avenues for exploring complex quantum many-body systems.

DOI: 10.1103/PhysRevLett.134.183406

Introduction—Interacting fermions form the foundation of diverse matter types, spanning vast energy and length scales, from materials and ultracold matter [1,2] to nuclei and neutron stars [3,4]. While spin populations are typically equal, imbalanced spin systems frequently occur in various physical systems. These systems have provided fundamental insights into exotic quantum phases, ranging from superconductivity under applied magnetic fields [5,6] to quark superfluidity in the early Universe [7]. Two-component ultracold fermions with spin imbalance, in particular, enable the study of numerous phenomena, including exotic superfluidity at unitarity [8–12], Fermi polarons [13,14], and Fulde-Ferrell-Larkin-Ovchinnikov states in 1D [15–18].

While conventional two-component fermionic systems with SU(2) symmetry constitute the building blocks of most matter, large spins with enhanced SU(N) symmetry promise novel quantum phenomena and insights. Recent advances in cold atom experiments and theory have realized such SU(N) many-body systems [19,20]. These include SU(N) Fermi liquids [21–28], SU(N) Mott insulators [29–34], BCS pairing in N-component systems [35–41], two-orbital SU(N) fermions [42–47], and antiferromagnetic correlations enhanced by SU(N) symmetry [42,48–50]. Studying thermodynamics, particularly measuring density fluctuations linked to isothermal compressibility through the fluctuation-dissipation theorem, has been crucial in characterizing SU(N) Fermi gases [51–54]. Experiments with deeply degenerate gases ($T/T_F \ll 1$) have shown reduced density fluctuations due to Pauli blocking [55–57]. In the spin-balanced limit, where each species has an equal population, mean-field theory predicts that interaction effects on thermodynamics are enhanced by a factor of $N-1$ [22,23,26,58]. However, the thermodynamic characterization of spin-imbalanced multicomponent fermions with SU(N) symmetric interaction has presented significant challenges due to the lack of systematic understanding of interaction enhancement in these systems.

In this Letter, we present systematic theoretical and experimental studies of density fluctuations in multicomponent Fermi gases with SU(N) symmetric interactions beyond the spin-balanced limit. We show that Hartree-Fock-type terms in the diagrammatic expansion are most enhanced in the large N limit. We provide closed-form formulas for calculating density fluctuations in Fermi gases with SU(N) symmetric interactions and spin-imbalanced configurations at finite temperatures. Experimentally, we utilize ^{173}Yb atoms to create deeply degenerate Fermi gases with SU(N) symmetric interactions. The number of species is highly

---

[*] These authors contributed equally to this work.
[†] Contact author: yqyan@cuhk.edu.hk
[‡] Contact author: gbjo@rice.edu

tunable from $N = 1$ to 6, with adjustable proportions in the total population. We first revisit the spin-balanced SU(N) fermions, calibrating density-fluctuation measurements in the $N = 1$ system and demonstrating agreement between our experiments and theory in the balanced SU(6) system. Next, we examine systems with imbalanced populations, specifically two-species and four-species configurations, validating our theoretical predictions for general setups. Leveraging our analytical expression, we also provide additional theoretical results supporting the fact that interaction enhancement effects can be significant in highly spin-imbalanced systems. Most notably, we observe a non-monotonic dependence of density fluctuations on spin population ratios originating from the complex interplay between particle statistics, interaction effects, and temperature. Finally, we apply density-fluctuation measurements to determine decoherence populations in our systems, which is qualitatively consistent with Ramsey-like measurements.

Experimental procedure—Figure 1(a) shows our experimental setup. We first produce a multicomponent degenerate Fermi gas via evaporative cooling in a crossed optical dipole trap (ODT) with two horizontal 1064 nm beams. Using optical pumping and a blast pulse [25], we prepare atom samples with balanced or imbalanced spin populations. To vary temperatures and densities, we adjust the final depth of the ODT. Finally, we calibrate the trap frequency of all three axes $\{\omega_1, \omega_2, \omega_3\}$ by measuring the dipole mode frequency of the atom cloud.

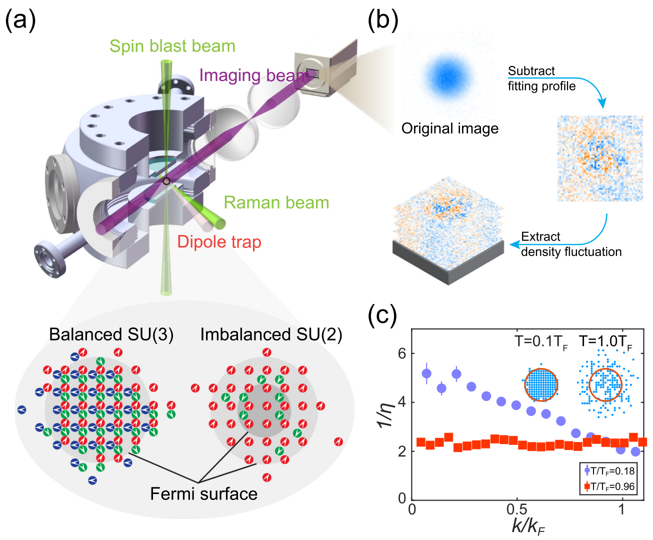

FIG. 1. Experimental setup for measurement of atom number variance. (a) Degenerate Fermi gases are prepared in a cross-dipole trap. Momentum distribution of Fermi gas samples is measured using absorption imaging after 20 ms TOF time. (b) We subtract a fitting profile for each image to counter total atom number fluctuation. (c) $1/\eta$ for thermal and degenerate Fermi gases at different k/k_F. Insets: schematics for state occupation status in the momentum space.

Spin configurations are calibrated with the optical Stern-Gerlach (OSG) effect; the inset of Fig. 2(b) shows typical OSG images of balanced SU(N). We then hold the atom cloud in ODT for 400 ms to reach thermal equilibrium, release the atoms, and after 20 ms free expansion take absorption images with a 3.76 magnification system.

Fluctuations calibration—Density fluctuation is measured by counting atom numbers in a small volume from repeated absorption images under the same conditions. We extract the averaged atom number N_0 and variance ΔN_0^2, calculating the variance per atom $\eta = \Delta N_0^2/N_0$. To achieve a high signal-to-noise ratio while keeping atom movement small enough during imaging, we set the exposure time to 40 μs. Because of our imaging system's aberrations and limited resolution (around 4 μm or 2 pixels), blurring occurs that reduces measured η values below theoretical predictions [59,60]. To mitigate, we use 7-pixel binning with an additional constant multiplication factor α (see End Matter). Prepared atomic samples exhibit fluctuations in atom number and temperature, affecting the extracted η. We subtract a Fermi fitting profile from each image to exclude these effects and calculate η from the subtracted images [61,62]. A raw and a subtracted image are shown in Fig. 1(b). Red squares and blue circles in Fig. 1(c) show the inverse variance versus momentum for thermal and degenerate Fermi gas, respectively.

Triangles and circles in Fig. 2(a) show the inverse local fluctuation of line-of-sight integrated density profiles measured at the trap center for SU(1) (i.e., noninteracting system) and SU(6) *spin-balanced* systems. For a noninteracting Fermi gas, it is expected to be $\eta = \alpha\{[\mathrm{Li}_1(-z_0)]/[\mathrm{Li}_2(-z_0)]\}$, where Li denotes polylogarithm functions. The fugacity z_0 is implicitly given by $-\mathrm{Li}_3(-z_0) = [(T_F^3)/(6T^3)]$,

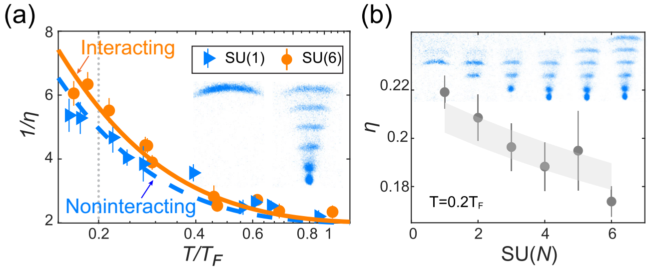

FIG. 2. Thermometry for interacting degenerate SU(N) fermions. (a) Inverse fluctuation $1/\eta$ as a function of T/T_F. The orange-solid (blue-dashed) line and orange circles (blue triangles) are the theoretical prediction of SU(6) [SU(1)] gas multiplied by a factor α and experimental data, respectively. The vertical dotted line denotes the deep-degeneracy temperature $T = 0.2T_F$ where data in (b) is measured. (b) Fluctuation η for SU(N) gases as a function of the number of component N. The shaded area is the theoretical prediction considering 5% uncertainty in temperature measurement.

where the Fermi temperature T_F is determined by $T_F = \hbar(\omega_1\omega_2\omega_3)^{\frac{1}{3}}(6N_0^s)^{\frac{1}{3}}$. $N_0^s = N_0/N$ refers to the number of spins of an arbitrary species. Factor α comes from the blurring effect [59,60] mentioned above. In our experiment, we extract $\alpha = 0.52(2)$ for the best fit (dashed line). For noninteracting $SU(1)$ gas, as the temperature goes down, the Pauli suppression effect becomes more evident, i.e., the number of available states decreases, and η decreases.

To validate the scaling factor α, we further compare the theoretical prediction scaled by α with the experimental data of SU(6) system. Since different spins exert weak repulsive interaction with scattering length $a_s k_F \simeq 0.1$ to each other, the expression of η of SU(1) system does not apply anymore. We derive that, for a *homogeneous* SU(N) Fermi gas, the density fluctuation is approximated by

$$\eta = \frac{-4(T/T_F^{\mathrm{hom}})^{3/2}\mathrm{Li}_{\frac{1}{2}}(-z_0^{\mathrm{hom}})}{3\sqrt{\pi} - 3(N-1)a_s k_F^{\mathrm{hom}}\sqrt{T/T_F^{\mathrm{hom}}}\mathrm{Li}_{\frac{1}{2}}(-z_0^{\mathrm{hom}})}, \quad (1)$$

where T_F^{hom}, k_F^{hom}, and z_0^{hom} are Fermi temperature, Fermi momentum, and noninteracting fugacity, respectively. Equation (1) is based on the Hartree-Fock approximation, which becomes exact in the large N limit. This is because, in the diagrammatic expansion, we inductively proved that Hartree-Fock terms of the grand potential get $N(N-1)^m$-fold enhancement at order m. At the same time, all other diagrams are only enhanced by $N(N-1)^{m'}$, where $m' < m$ [63]. Our theoretical predictions are valid in the weak-interaction regime $|a_s k_F^{\mathrm{hom}}| \ll 1$ [63]. For repulsive interactions ($a_s > 0$), Eq. (1) remains accurate for all accessible N values due to the convergence of the perturbative series and dominance of Hartree-Fock diagrams. For attractive interactions ($a_s < 0$), stability requires $N < \pi/(2|a_s k_F^{\mathrm{hom}}|) + 1$ to avoid collapse into a liquid phase. It can be checked that in the zero-temperature limit $T/T_F^{\mathrm{hom}} \to 0$, Eq. (1) recovers the well-known relation $\eta = \frac{3}{2}\{[T/T_F^{\mathrm{hom}}]/[1 + (2/\pi)(N-1)k_F^{\mathrm{hom}}a_s]\}$ [22,26,28]. To apply Eq. (1) to our system, we perform a local-density approximation and integrate along the line of sight of imaging. Further multiplied by the aforementioned scaling factor $\alpha = 0.52$, our theory [red solid line in Fig. 2(a)] agrees well with the experimental data (circles). Compared with SU(1) gas, the fluctuation for SU(6) Fermi gas is even lower due to repulsive interaction, and the effect is more pronounced in the deeply degenerate region. Besides temperature, it is clear that the total number of species N also influences the interaction effect. Figure 2(b) demonstrates how the fluctuation reduces as we gradually increase N from 1 to 6. All samples are prepared with approximately the same temperature $T/T_F \simeq 0.2$. At this temperature, η for SU(6) gas is 16% lower than for SU(1) gas.

Spin-imbalanced gases—With fluctuation calibration completed using spin-balanced systems, we now examine spin-imbalanced systems, where numbers of particles in each spin are $N_0^{(\sigma)} = \xi_\sigma N_0^s$; N_0^s represents the number of particles for the majority spin and $\xi_1 = 1$. To investigate the influence of an imbalanced population on the system, we study the number fluctuation of SU(N) system when "N" is smoothly tuned, by which we mean we change $\sum_\sigma \xi_\sigma$ from N to a different value.

We experimentally study the fluctuation in two schemes in the deep quantum degeneracy regime, $T/T_F = 0.2$: crossover from SU(1) to SU(2) gases by modifying ξ_2 from 0 to 1 [circles in Fig. 3(a)] and crossover from SU(2) to SU(4) by simultaneously modifying ξ_3 and ξ_4 from 0 to 1 while keeping $\xi_2 = \xi_1 = 1$ [circles in Fig. 3(b)]. We observe a nonmonotonic dependence of fluctuation on the number of particles. The quick increase in the highly spin-imbalanced regime is because, at a given global equilibrium temperature T, the Fermi temperature for the minority populations is smaller, resulting in higher T/T_F ratios. This leads to larger fluctuations in minority particles, increasing overall averaged local fluctuations. Meanwhile, a larger N suppresses fluctuation due to the interaction effect, which is consistent with our analysis of balanced systems. We obtain an analytical formula describing the feature,

$$\eta = \frac{-3\pi}{4a_s k_F^{\mathrm{hom}}\sum_\sigma \xi_\sigma}\frac{T}{T_F^{\mathrm{hom}}}\frac{(\sum_\sigma g_\sigma)^2}{\sum_\sigma g_\sigma(1 - \sum_{\sigma'\neq\sigma} g_{\sigma'})}, \quad (2)$$

where

$$g_\sigma = \frac{a_s k_F^{\mathrm{hom}} T^{\frac{1}{2}}}{\sqrt{\pi}(T_F^{\mathrm{hom}})^{\frac{1}{2}}}\mathrm{Li}_{\frac{1}{2}}\left[\mathrm{Li}_{\frac{3}{2}}^{-1}\left(-\frac{4\xi_\sigma (T_F^{\mathrm{hom}})^{\frac{3}{2}}}{3\sqrt{\pi}T^{\frac{3}{2}}}\right)\right] \quad (3)$$

where $^{-1}$ denotes the inverse function. When $\xi_\sigma = 1$ for all possible σ, Eq. (2) reduces to Eq. (1). By comparing with experimental results, especially in Fig. 3(b) where the interaction effect is pronounced, Eq. (2) under local-density approximation with factor α is shown to explain the experimental data much better than calculations ignoring interaction effects. The minor discrepancy observed near the SU(1) limit in Fig. 3(a), $\xi_\sigma - 1 \lessapprox 0.1$, may be attributed to two factors: unstable experimental control of the population ratio and the reduced accuracy of the Hartree-Fock approximation in this regime. This "polaron physics" regime [65] may be better described with more diagrams included.

After comparing with experimental data, we further emphasize the importance of Eq. (2) by presenting theoretical results in a homogeneous system. Figure 3(c) shows the change of η as the SU(1) gas is smoothly tuned to the SU(6) limit by changing ξ_σ for $\sigma = 2, \ldots, 6$ from 0 to 1 *one by one*. Solid and dashed lines in the upper panel show the

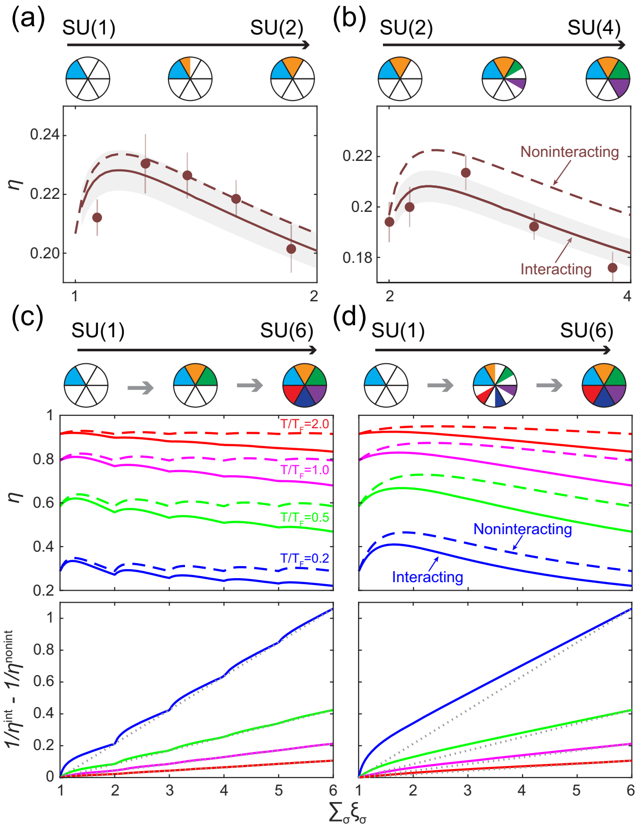

FIG. 3. Density fluctuation η of spin-imbalanced systems. (a) Circles show the experimental data of η as a function of $\sum_\sigma \xi_\sigma$, with varying ξ_2 from 0 to 1. Solid lines and dashed lines show the theoretical prediction of an interacting and noninteracting system, respectively, with $a_s k_F = 0.1$ and $T/T_F = 0.2$. The shaded areas denote the error considering 3% temperature uncertainty. (b) Comparing to (a), instead of varying ξ_2, ξ_3, and ξ_4 are simultaneously changed from 0 to 1 while ξ_2 and ξ_1 are kept at 1. (c) Theoretical predictions of η in homogeneous systems without correcting factor α based on Eq. (2). The upper panel shows how η changes when ξ_σ for $\sigma = 2, \ldots, 6$ are tuned from 0 to 1 *one by one* as illustrated by the chart schematic. Solid lines are results of interacting systems η^{int} with $a_s k_F^{\text{hom}} = 0.1$, while dashed lines are η^{nonint} for noninteracting systems with $a_s k_F^{\text{hom}} = 0$. The solid line in the lower panel shows the difference in the inverse fluctuation between interacting and noninteracting systems. The dotted lines show a naive generalization of results from spin-balanced systems. (d) Same plot as (c), except that $\sigma = 2, \ldots, 6$ are tuned from 0 to 1 *simultaneously.*

fluctuation of interacting systems η^{int} and noninteracting systems η^{nonint}, respectively. We observe that the difference increases as the total spin increases. Based on Eq. (1), the $(N-1)a_s$ interaction enhancement in spin-balanced SU(N) gases is also applicable to the inverse fluctuation, i.e., $1/\eta^{\text{int}} - 1/\eta^{\text{nonint}} \propto (N-1) a_s k_F^{\text{hom}} T_F^{\text{hom}}/T$. The dashed lines (dotted lines in the lower panel) show our naive generalization $[(\sum_\sigma \xi_\sigma) - 1) a_s k_F^{\text{hom}}] T_F^{\text{hom}}/T$ to the spin-imbalanced systems. In comparison, the solid lines show the inverse change of fluctuation based on Eq. (2). They agree well at high temperatures and differ slightly at low temperatures.

Changing the scheme to create the spin imbalance brings us even more interesting results. In Fig. 3(d), we tune all $\xi_{\sigma>2}$ *simultaneously* from 0 to 1 and show the same quantities. In the upper panel, we observe a clear increase in the difference of fluctuations of the interacting (solid lines) and noninteracting (dashed lines) systems at high temperatures ($T/T_F^{\text{hom}} = 2$ and $T/T_F^{\text{hom}} = 1$). However, in deep degeneracy regimes ($T/T_F^{\text{hom}} = 0.2$), the difference saturates at $\sum_\sigma \xi_\sigma \approx 2$, where each minor species approximately has only 10% of the major population. Similarly, in the lower panel, comparing to the change of inverse fluctuation in the previous case, we obverse a much more prominent difference between the results based on Eq. (2) and the naive generalization, especially when the minor-major spin ratio is around 10%. This generalized SU(N) interaction enhancement suggests that compared to the interaction energy, the fluctuation is much more sensitive to the scattering length at sufficiently low temperatures, especially in highly imbalanced population setups.

Application of fluctuation measurement: Determining decoherence—Understanding how an imbalanced population can affect density fluctuation allows us to reveal the decoherence dynamics in SU(N) Fermi gases [66–69]. We first prepare a spin-polarized SU(1) Fermi gas in equilibrium, then apply a Raman pulse to suddenly rotate the spin to an equal superposition of N spin states. Initially, one expects each spin to be rotated to the same superposition state [Fig. 4(a)], and the fluctuation should be kept the same as the SU(1) case. In the long time limit, the fluctuation of gas approaches that of an SU(N) gas due to the spin decoherence, whose mechanism is sophisticated, including various interaction-induced effects [43,70] as well as the inhomogeneity of laser intensity across the trap. In between, we interpolate the population ratios from SU(1) to SU(N), i.e., $(\xi_1, \xi_2, \ldots, \xi_N) = \{1 - [(N-1)/N]\zeta, (\zeta/N), \ldots, (\zeta/N)\}$, where ζ denotes the ratio of population of decoherence. That is, we treat systems after decoherence as imbalanced SU(N) Fermi gases discussed previously and apply Eq. (2) with local-density approximation to calculate the fluctuations. We calculate and show in Fig. 4(b) that η increases with ζ at $T/T_F \sim 0.2$, where T_F is calculated using $N_0^{(1)}$ at $t = 0$. While this may seem to contradict the lower η observed for balanced SU(N) gases (Fig. 2), the effect arises from the reduction of effective T_F *for each species* to $T_F^\infty = T_F/N$ in the asymptotic limit. This leads to a higher effective temperature T/T_F^∞ with T unchanged [see inset of Fig. 4(d)] that dominates over interaction effects, resulting in enhanced density fluctuations. Experimentally, we measure the density fluctuation for different holding times after spin rotation. Squares, triangles, and circles with error bars in

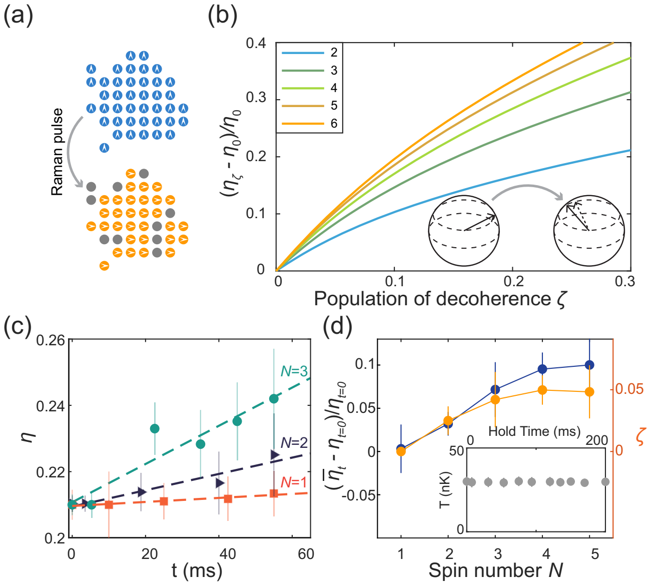

FIG. 4. Density fluctuation during spin decoherence. (a) A schematic showing the Raman pulse changes the gas in a single spin state to a coherent spin state, followed by decoherence. (b) Relative difference in variance per atom η between the postdecoherence state η_ζ and initial state η_0 for quenching to different $N = (2, 3, \ldots, 6)$ at temperature $T = 0.2T_F$ [based on Eq. (2)]. (c) Experimental measurement of η for spin-polarized gas quench to spin N state (N from 1 to 3). Dashed lines are linear fits. (d) Relative difference in fluctuation (blue symbols) and estimated decoherence (orange symbols) averaged over a period from 40 to 100 ms. Inset: circles show the fitted temperatures as a function of the holding time.

Fig. 4(c) show the fluctuation for spin number $N = 1, 2, 3$, respectively, as a function of holding time. We observe that the fluctuation increases faster when N is larger. Blue and orange circles in Fig. 4(d) show the relative change of fluctuations and decoherence estimated based on Fig. 4(b) averaged between 40 and 100 ms holding time as a function of spin number. We find a <10% increase of η after the Raman pulse for $N = 5$. This change in density fluctuation corresponds to around ~5% atoms undergoing decoherence (qualitatively confirmed by double-pulse Ramsey-like spectroscopy; see End Matter).

Conclusion—To summarize, we have examined density fluctuations in multicomponent Fermi gases with SU(N) symmetric interactions, providing analytical formulas for general spin-imbalanced configurations and demonstrating agreement between theory and experiments with ^{173}Yb atoms. This Letter establishes a foundation for studying quantum systems across various fields, from condensed matter physics to quantum chromodynamics, where understanding the thermodynamics of multicomponent systems with imbalanced populations is crucial. As an immediate application, we have demonstrated how density-fluctuation measurements can be used to monitor decoherent populations, establishing crucial fluctuation-based thermometry for multicomponent Fermi gases. Our results open new possibilities for exploring physics in imbalanced multicomponent systems, such as the multicomponent polaron problem. Furthermore, by combining orbital Feshbach resonance with oscillating magnetic fields [71,72], we could potentially achieve strong interactions between one spin component and several others. This approach could further enhance the interaction effects and help drive the gas into the superfluid regime.

Acknowledgments—This work is supported by C4050-23G. G. B. J. also acknowledges support from the Research Grants Committee (RGC) through 16302420, 16302821, 16306321, 16306922, 16302123, C6009-20G, N-HKUST636-22, and RFS2122-6S04. Y. Y. acknowledges support from the RGC through 24308323, NSFC through 12204395, and the Space Application System of China Manned Space Program. C. H. acknowledges support from the RGC for the RGC Postdoctoral fellowship.

[1] I. Bloch, J. Dalibard, and W. Zwerger, Many-body physics with ultracold gases, Rev. Mod. Phys. **80**, 885 (2008).

[2] M. Inguscio, W. Ketterle, and C. Salomon, *Ultra-Cold Fermi Gases* (IOS Press, Amsterdam, 2008), Vol. 164.

[3] D. Bailin and A. Love, Superfluidity and superconductivity in relativistic fermion systems, Phys. Rep. **107**, 325 (1984).

[4] R. Casalbuoni and G. Nardulli, Inhomogeneous superconductivity in condensed matter and QCD, Rev. Mod. Phys. **76**, 263 (2004).

[5] C. H. L. Quay, D. Chevallier, C. Bena, and M. Aprili, Spin imbalance and spin-charge separation in a mesoscopic superconductor, Nat. Phys. **9**, 84 (2013).

[6] J. Linder and J. W. A. Robinson, Superconducting spintronics, Nat. Phys. **11**, 307 (2015).

[7] M. G. Alford, A. Schmitt, K. Rajagopal, and T. Schäfer, Color superconductivity in dense quark matter, Rev. Mod. Phys. **80**, 1455 (2008).

[8] M. W. Zwierlein, A. Schirotzek, C. H. Schunck, and W. Ketterle, Fermionic superfluidity with imbalanced spin populations, Science **311**, 492 (2006).

[9] G. B. Partridge, W. Li, R. I. Kamar, Y.-A. Liao, and R. G. Hulet, Pairing and phase separation in a polarized Fermi gas, Science **311**, 503 (2006).

[10] J. Kinnunen, L. M. Jensen, and P. Törmä, Strongly interacting Fermi gases with density imbalance, Phys. Rev. Lett. **96**, 110403 (2006).

[11] L. Radzihovsky and D. E. Sheehy, Imbalanced Feshbach-resonant Fermi gases, Rep. Prog. Phys. **73**, 076501 (2010).

[12] K. B. Gubbels and H. T. C. Stoof, Imbalanced Fermi gases at unitarity, Phys. Rep. **525**, 255 (2013).

[13] M. Punk, P. T. Dumitrescu, and W. Zwerger, Polaron-to-molecule transition in a strongly imbalanced Fermi gas, Phys. Rev. A **80**, 053605 (2009).

[14] C. Mora and F. Chevy, Normal phase of an imbalanced Fermi gas, Phys. Rev. Lett. **104**, 230402 (2010).

[15] H. Hu, X.-J. Liu, and P. D. Drummond, Phase diagram of a strongly interacting polarized Fermi gas in one dimension, Phys. Rev. Lett. **98**, 070403 (2007).

[16] M. Rizzi, M. Polini, M. A. Cazalilla, M. R. Bakhtiari, M. P. Tosi, and R. Fazio, Fulde-Ferrell-Larkin-Ovchinnikov pairing in one-dimensional optical lattices, Phys. Rev. B **77**, 245105 (2008).

[17] M. Tezuka and M. Ueda, Density-matrix renormalization group study of trapped imbalanced Fermi condensates, Phys. Rev. Lett. **100**, 110403 (2008).

[18] Y.-a. Liao, A. S. C. Rittner, T. Paprotta, W. Li, G. B. Partridge, R. G. Hulet, S. K. Baur, and E. J. Mueller, Spin-imbalance in a one-dimensional Fermi gas, Nature (London) **467**, 567 (2010).

[19] C. He, E. Hajiyev, Z. Ren, B. Song, and G.-B. Jo, Recent progresses of ultracold two-electron atoms, J. Phys. B **52**, 102001 (2019).

[20] E. Ibarra-García-Padilla and S. Choudhury, Many-body physics of ultracold alkaline-Earth atoms with SU(N)-symmetric interactions, J. Phys. Condens. Matter **37**, 083003 (2025).

[21] G. Y. Chitov and D. Sénéchal, Renormalization-group study of interacting electrons, Phys. Rev. B **52**, 13487 (1995).

[22] S.-K. Yip, B.-L. Huang, and J.-S. Kao, Theory of SU(N) Fermi liquids, Phys. Rev. A **89**, 043610 (2014).

[23] C.-H. Cheng and S.-K. Yip, SU(N) Fermi liquid at finite temperature, Phys. Rev. A **95**, 033619 (2017).

[24] C. He, Z. Ren, B. Song, E. Zhao, J. Lee, Y.-C. Zhang, S. Zhang, and G.-B. Jo, Collective excitations in two-dimensional SU(N) Fermi gases with tunable spin, Phys. Rev. Res. **2**, 012028(R) (2020).

[25] B. Song, Y. Yan, C. He, Z. Ren, Q. Zhou, and G.-B. Jo, Evidence for bosonization in a three-dimensional gas of SU(N) fermions, Phys. Rev. X **10**, 041053 (2020).

[26] L. Sonderhouse, C. Sanner, R. B. Hutson, A. Goban, T. Bilitewski, L. Yan, W. R. Milner, A. M. Rey, and J. Ye, Thermodynamics of a deeply degenerate SU(N)-symmetric Fermi gas, Nat. Phys. **16**, 1216 (2020).

[27] S. Choudhury, K. R. Islam, Y. Hou, J. A. Aman, T. C. Killian, and K. R. A. Hazzard, Collective modes of ultracold fermionic alkaline-Earth-metal gases with SU(N) symmetry, Phys. Rev. A **101**, 053612 (2020).

[28] E. Zhao, J. Lee, C. He, Z. Ren, E. Hajiyev, J. Liu, and G.-B. Jo, Heuristic machinery for thermodynamic studies of SU(N) fermions with neural networks, Nat. Commun. **12**, 2011 (2021).

[29] R. Assaraf, P. Azaria, M. Caffarel, and P. Lecheminant, Metal-insulator transition in the one-dimensional SU(N) Hubbard model, Phys. Rev. B **60**, 2299 (1999).

[30] S. Taie, R. Yamazaki, S. Sugawa, and Y. Takahashi, An SU(6) Mott insulator of an atomic Fermi gas realized by large-spin Pomeranchuk cooling, Nat. Phys. **8**, 825 (2012).

[31] P. Nataf, M. Lajkó, A. Wietek, K. Penc, F. Mila, and A. M. Läuchli, Chiral spin liquids in triangular-lattice SU(N) fermionic Mott insulators with artificial gauge fields, Phys. Rev. Lett. **117**, 167202 (2016).

[32] C. Hofrichter, L. Riegger, F. Scazza, M. Höfer, D. R. Fernandes, I. Bloch, and S. Fölling, Direct probing of the Mott crossover in the SU(N) Fermi-Hubbard model, Phys. Rev. X **6**, 021030 (2016).

[33] Z. Zhou, D. Wang, Z. Y. Meng, Y. Wang, and C. Wu, Mott insulating states and quantum phase transitions of correlated SU($2N$) Dirac fermions, Phys. Rev. B **93**, 245157 (2016).

[34] D. Wang, L. Wang, and C. Wu, Slater and Mott insulating states in the SU(6) Hubbard model, Phys. Rev. B **100**, 115155 (2019).

[35] A. G. K. Modawi and A. J. Leggett, Some properties of a spin-1 Fermi superfluid: Application to spin-polarized ^{6}Li, J. Low Temp. Phys. **109**, 625 (1997).

[36] C. Honerkamp and W. Hofstetter, BCS pairing in Fermi systems with N different hyperfine states, Phys. Rev. B **70**, 094521 (2004).

[37] L. He, M. Jin, and P. Zhuang, Superfluidity in a three-flavor Fermi gas with SU(3) symmetry, Phys. Rev. A **74**, 033604 (2006).

[38] Á. Rapp, G. Zaránd, C. Honerkamp, and W. Hofstetter, Color superfluidity and “baryon” formation in ultracold fermions, Phys. Rev. Lett. **98**, 160405 (2007).

[39] R. W. Cherng, G. Refael, and E. Demler, Superfluidity and magnetism in multicomponent ultracold fermions, Phys. Rev. Lett. **99**, 130406 (2007).

[40] T. Ozawa and G. Baym, Population imbalance and pairing in the BCS-BEC crossover of three-component ultracold fermions, Phys. Rev. A **82**, 063615 (2010).

[41] S.-K. Yip, Theory of a fermionic superfluid with SU(2) × SU(6) symmetry, Phys. Rev. A **83**, 063607 (2011).

[42] A. V. Gorshkov, M. Hermele, V. Gurarie, C. Xu, P. S. Julienne, J. Ye, P. Zoller, E. Demler, M. D. Lukin, and A. M. Rey, Two-orbital SU(N) magnetism with ultracold alkaline-Earth atoms, Nat. Phys. **6**, 289 (2010).

[43] X. Zhang, M. Bishof, S. L. Bromley, C. V. Kraus, M. S. Safronova, P. Zoller, A. M. Rey, and J. Ye, Spectroscopic observation of SU(N)-symmetric interactions in Sr orbital magnetism, Science **345**, 1467 (2014).

[44] F. Scazza, C. Hofrichter, M. Höfer, P. C. De Groot, I. Bloch, and S. Fölling, Observation of two-orbital spin-exchange interactions with ultracold SU(N)-symmetric fermions, Nat. Phys. **10**, 779 (2014).

[45] V. Bois, S. Capponi, P. Lecheminant, M. Moliner, and K. Totsuka, Phase diagrams of one-dimensional half-filled two-orbital SU(N) cold fermion systems, Phys. Rev. B **91**, 075121 (2015).

[46] V. Bois, P. Fromholz, and P. Lecheminant, One-dimensional two-orbital SU(N) ultracold fermionic quantum gases at incommensurate filling: A low-energy approach, Phys. Rev. B **93**, 134415 (2016).

[47] H. Ueda, T. Morimoto, and T. Momoi, Symmetry protected topological phases in two-orbital SU(4) fermionic atoms, Phys. Rev. B **98**, 045128 (2018).

[48] M. A. Cazalilla, A. F. Ho, and M. Ueda, Ultracold gases of ytterbium: Ferromagnetism and Mott states in an SU(6) Fermi system, New J. Phys. **11**, 103033 (2009).

[49] K. Tamura and H. Katsura, Ferromagnetism in the SU(n) Hubbard model with a nearly flat band, Phys. Rev. B **100**, 214423 (2019).

[50] S. Taie, E. Ibarra-García-Padilla, N. Nishizawa, Y. Takasu, Y. Kuno, H.-T. Wei, R. T. Scalettar, K. R. A. Hazzard, and Y. Takahashi, Observation of antiferromagnetic correlations in an ultracold SU(N) Hubbard model, Nat. Phys. **18**, 1356 (2022).

[51] E. R. Anderson and J. E. Drut, Pressure, compressibility, and contact of the two-dimensional attractive Fermi gas, Phys. Rev. Lett. **115**, 115301 (2015).

[52] Y.-R. Lee, M.-S. Heo, J.-H. Choi, T. T. Wang, C. A. Christensen, T. M. Rvachov, and W. Ketterle, Compressibility of an ultracold Fermi gas with repulsive interactions, Phys. Rev. A **85**, 063615 (2012).

[53] G. E. Astrakharchik, R. Combescot, and L. P. Pitaevskii, Fluctuations of the number of particles within a given volume in cold quantum gases, Phys. Rev. A **76**, 063616 (2007).

[54] G. Pasqualetti, O. Bettermann, N. Darkwah Oppong, E. Ibarra-García-Padilla, S. Dasgupta, R. T. Scalettar, K. R. A. Hazzard, I. Bloch, and S. Fölling, Equation of state and thermometry of the 2D SU(N) Fermi-Hubbard model, Phys. Rev. Lett. **132**, 083401 (2024).

[55] C. Sanner, E. J. Su, A. Keshet, R. Gommers, Y.-i. Shin, W. Huang, and W. Ketterle, Suppression of density fluctuations in a quantum degenerate Fermi gas, Phys. Rev. Lett. **105**, 040402 (2010).

[56] T. Müller, B. Zimmermann, J. Meineke, J.-P. Brantut, T. Esslinger, and H. Moritz, Local observation of antibunching in a trapped Fermi gas, Phys. Rev. Lett. **105**, 040401 (2010).

[57] W. G. Tobias, K. Matsuda, G. Valtolina, L. De Marco, J.-R. Li, and J. Ye, Thermalization and sub-Poissonian density fluctuations in a degenerate molecular Fermi gas, Phys. Rev. Lett. **124**, 033401 (2020).

[58] M. A. Cazalilla and A. M. Rey, Ultracold Fermi gases with emergent SU(N) symmetry, Rep. Prog. Phys. **77**, 124401 (2014).

[59] J. Esteve, J.-B. Trebbia, T. Schumm, A. Aspect, C. I. Westbrook, and I. Bouchoule, Observations of density fluctuations in an elongated Bose gas: Ideal gas and quasicondensate regimes, Phys. Rev. Lett. **96**, 130403 (2006).

[60] N. Gemelke, X. Zhang, C.-L. Hung, and C. Chin, In situ observation of incompressible Mott-insulating domains in ultracold atomic gases, Nature (London) **460**, 995 (2009).

[61] Q. Chen, C. A. Regal, D. S. Jin, and K. Levin, Finite-temperature momentum distribution of a trapped Fermi gas, Phys. Rev. A **74**, 011601(R) (2006).

[62] D. A. Butts and D. S. Rokhsar, Trapped Fermi gases, Phys. Rev. A **55**, 4346 (1997).

[63] See Supplemental Material at http://link.aps.org/supplemental/10.1103/PhysRevLett.134.183406 for details on the formalism of calculating density fluctuation of homogeneous systems and the method of performing the line-of-sight integration, which includes Ref. [64].

[64] A. L. Fetter and J. D. Walecka, *Quantum Theory of Many-Particle Systems* (Courier Corporation, New York, 2012).

[65] P. Massignan, M. Zaccanti, and G. M. Bruun, Polarons, dressed molecules and itinerant ferromagnetism in ultracold Fermi gases, Rep. Prog. Phys. **77**, 034401 (2014).

[66] R. J. Fletcher, R. Lopes, J. Man, N. Navon, R. P. Smith, M. W. Zwierlein, and Z. Hadzibabic, Two- and three-body contacts in the unitary Bose gas, Science **355**, 377 (2017).

[67] M. Cetina, M. Jag, R. S. Lous, I. Fritsche, J. T. M. Walraven, R. Grimm, J. Levinsen, M. M. Parish, R. Schmidt, M. Knap, and E. Demler, Ultrafast many-body interferometry of impurities coupled to a Fermi sea, Science **354**, 96 (2016).

[68] A. B. Bardon, S. Beattie, C. Luciuk, W. Cairncross, D. Fine, N. S. Cheng, G. J. A. Edge, E. Taylor, S. Zhang, S. Trotzky, and J. H. Thywissen, Transverse demagnetization dynamics of a unitary Fermi gas, Science **344**, 722 (2014).

[69] S. Gupta, Z. Hadzibabic, M. W. Zwierlein, C. A. Stan, K. Dieckmann, C. H. Schunck, E. G. M. van Kempen, B. J. Verhaar, and W. Ketterle, Radio-frequency spectroscopy of ultracold fermions, Science **300**, 1723 (2003).

[70] U. Ebling, J. S. Krauser, N. Fläschner, K. Sengstock, C. Becker, M. Lewenstein, and A. Eckardt, Relaxation dynamics of an isolated large-spin Fermi gas far from equilibrium, Phys. Rev. X **4**, 021011 (2014).

[71] R. Zhang, Y. Cheng, H. Zhai, and P. Zhang, Orbital Feshbach, resonance in alkali-Earth atoms, Phys. Rev. Lett. **115**, 135301 (2015).

[72] G. Cappellini, L. F. Livi, L. Franchi, D. Tusi, D. Benedicto Orenes, M. Inguscio, J. Catani, and L. Fallani, Coherent manipulation of orbital Feshbach molecules of two-electron atoms, Phys. Rev. X **9**, 011028 (2019).

End Matter

Atom Sample Preparation and Calibration—We produce a degenerate Fermi gas through evaporative cooling in an ODT [Fig. 5(b)]. The temperature of the atom sample is controlled by tuning the final ODT depth V_0. Samples with different spin configurations are prepared by combining spin pumping and blast. Pumping beam wavelength is near 399 nm red detuned 400 MHz from ${}^1\mathrm{S}_0$–${}^1\mathrm{P}_1$ transition with $\sigma+$ polarization. The spin blast beam is 556 nm, resonance frequency of narrow line ${}^1\mathrm{S}_0$–${}^3\mathrm{P}_1$ transition with both $\sigma+$ and $\sigma-$ polarization. After preparing a specific spin configuration, we hold atoms in the trap for 400 ms to reach thermal equilibrium. We use a Raman beam, which is 1 GHz blue detuned from ${}^1\mathrm{S}_0$–${}^3\mathrm{P}_1$ transition with mix π and horizontal linear polarization, to flip atom spin. We switch off ODT and let the atom cloud expand freely for 20 ms before absorption imaging. To reduce fringes in the absorption image, we use a short interframe time between the first and reference image within 200 μs. We use a resonance 399 nm blast beam between two frames to blow the atom cloud away from the image area.

ODT trap geometry is calibrated by measuring dipole mode frequency as shown in Fig. 5(a). We quench ODT trap depth to trigger the vertical motion of the atom cloud and use an optical Stern-Gerlach beam to give atoms momentum kick in the horizontal direction. A typical value of our trap frequency is $\{(\omega_1, \omega_2, \omega_3)\} = \{84, 46, 143\} \times 2\pi$ Hz.

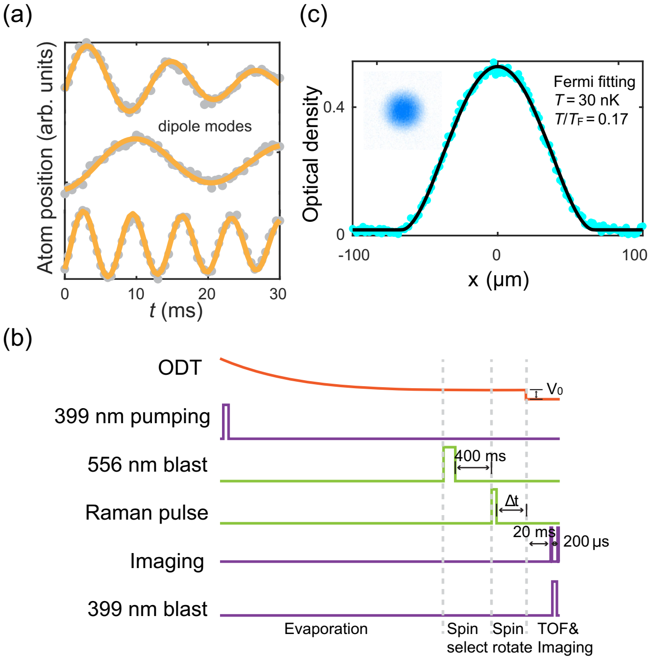

FIG. 5. Experimental sequence. (a) ODT trap frequency calibration $\{(\omega_1, \omega_2, \omega_3)\} = \{84, 46, 143\} \times 2\pi$ Hz. (b) The temperature of the atomic sample is controlled by varying final ODT depth V_0. Different spin configurations are prepared using 399 nm pumping and 556 nm blast pulse; atoms are held in ODT for 400 ms to reach thermal equilibrium before measurement. A Raman pulse is used to flip spin in quench dynamics measurement. Short interframe time absorption imaging is applied to measure atom distribution after 20 ms time of flight. The interframe time is 200 μs, and a 399 nm blast pulse is applied to clean all atoms between two frames. (c) The atom cloud profile is fitted with the Fermi-Dirac distribution function to determine the temperature.

Fermi temperature is $T_F = \frac{\hbar}{k_B}\sqrt[3]{\omega_1\omega_2\omega_3 \times 6N_0^{(1)}}$. We extract temperature by fitting the atom cloud profile with Fermi-Dirac distribution as shown in Fig. 5(c). This method is accurate for noninteracting samples; it will overestimate the temperature no more than 1.5% for weakly interacting samples in our case.

Noise in the absorption image from photon shot or camera readout noise will affect extraction atom number variance. To eliminate those effects, except for variance within the region of interest, we also extract the total variance for areas far away from the atom cloud as background, where almost no atom exists. We take the variance value after subtracting the background for each sample set. Figure 6(a) shows a typical atom number and its variance versus distance from the atom cloud center with two gray areas marked as the region of interest and background area correspondingly.

Because of the imperfection of the imaging system, binning size will affect the extracted variance value, as shown in Fig. 6(b). We bin raw data with specific sizes to reduce these effects. Meanwhile, the bin size cannot be too large due to the limited atom cloud size. We find the variance ratio between degenerate and thermal gases approaches a constant value as the bin size exceeds 7 pixels. At that binning size, the extracted variance reflects the actual value of different samples with a constant factor. For all data presented in this Letter, we use the 7-pixel bin.

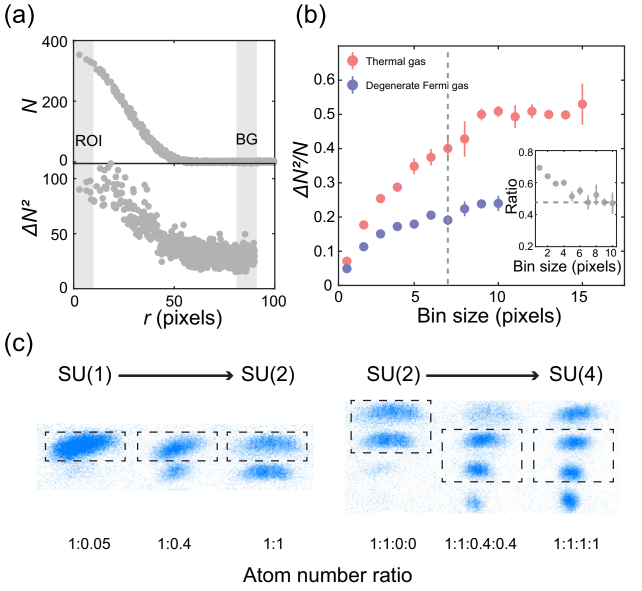

FIG. 6. Imaging system calibration and Optical Stern-Gerlach measurements. (a) The upper panel shows the average atom number in one binning area, and the x axis is the distance away from the center of the atom cloud. The lower panel is the total variance. At the area far from the center, where there are almost no atoms, total variance is a constant value contributed by photon shot noise, readout noise, and dark noise. The shaded region on the left indicates density fluctuation at the center of the atom cloud; the shaded region on the right acts as a background. (b) Variance per atom when taking different bin sizes with the same datasets. When the bin size is large enough, variances tend to be constant. The inset plot shows the variance ratio between degenerate Fermi gas and thermal gas. (c) The atom number in each spin state is examined through optical Stern-Gerlach measurement. We can prepare arbitrary spin configurations by tuning the spin pumping and blast beam power. The left part shows an imbalanced two-spin Fermi gas with a tunable atom number ratio. The right part shows a four-spin Fermi gas with two major and two minor spin components.

By carefully tuning blast beam power for each spin state, we can prepare balanced and imbalanced spin configurations. The preparation result can be examined by counting atom number after OSG pulse as shown in Fig. 1(c).

In the experiment, we quench atom spin using a Raman pulse. We rotate the spin of spin-polarized atoms to superposition states of N spin. We can change the superposition states by tuning the power, the power ratio between π, and linear polarization and pulse time of the Raman beam. The coefficient of each spin component is nearly the same (within 10% difference) as shown in Fig. 7(a). We use a Ramsey spectroscopy to test the coherence of the atom sample. For a two-spin system, the first $\pi/2$ pulse will flip the spin from $|\uparrow\rangle$ to $(|\uparrow\rangle + |\downarrow\rangle)/\sqrt{2}$, after a waiting time δt, the second $\pi/2$ will rotate to a δt dependent superposition states of spin-up and spin-down if there is no decoherence. For spin $N = 6$ system, the first $\pi/2$ pulse will rotate spin from $|m_F = 5/2\rangle$ to $|m_F = 5/2\rangle + |m_F = 3/2\rangle$ usually with a small fraction of $|m_F = 1/2\rangle$ as plotted in Fig. 7. The second pulse will rotate spin to the superposition of all six spin states depending on interpulse waiting time δt. If the system keeps fully coherent for a certain waiting time, the spin can return to $|m_F = 5/2\rangle$. However, if there is decoherence, the contrast of spin oscillation will drop as shown in Fig. 7(b). If the system becomes fully decoherent, the final states after the second $\pi/2$ pulse will be time-independent. According to our Ramsey-like spectroscopy up to 100 ms hold time, the spin population oscillates as expected in a coherent sample [Fig. 7(b)] with large contrast, which suggests the system remains almost coherent within 100 ms [Fig. 7(c)]. A typical Ramsey sequence can be used to quantitatively determine the decoherent population by investigating how the envelope of the oscillation decays. However, it is noted that since the decoherent ratio is small (typically <10%), such an approach is limited by the non-negligible noise observed in the longer time.

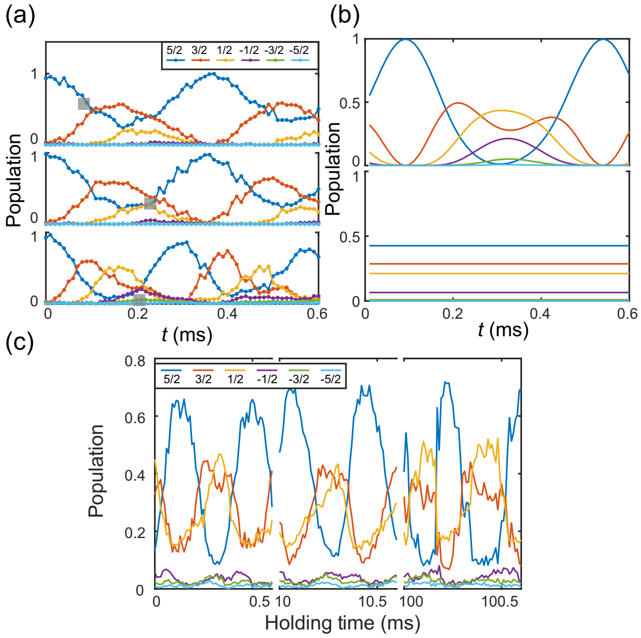

FIG. 7. Rabi oscillation during quench dynamics. (a) Rabi oscillation for quench pulse from spin-polarized Fermi gases to near equally distributed 2-, 3-, 4-spin Fermi gases. We truncate Rabi oscillation at a gray square. Higher Raman pulse power is required for transitions to larger spin-number states. (b) Theoretical predictions of atom population after $\pi/2$ pulse for a coherent gas (upper panel) and decoherent gas (lower panel) start from a SU(2) Fermi gas. (c) Spin population measurement after a Ramsey-like sequence—two $\pi/2$ pulses for different interpulse holding time. Rabi frequency between $m_F = 3/2$ and $m_F = 5/2$ is around 5 kHz.